

Unveiling Local Electronic Structure of Lanthanide-Doped Cs₂NaInCl₆ Double Perovskites for Realizing Efficient Near-Infrared Luminescence

Siyuan Han, Datao Tu,* Zhi Xie, Yunqin Zhang, Jiayao Li, Yifan Pei, Jin Xu, Zhongliang Gong, and Xueyuan Chen*

Lanthanide ion (Ln³⁺)-doped halide double perovskites (DPs) have evoked tremendous interest due to their unique optical properties. However, Ln³⁺ ions in these DPs still suffer from weak emissions due to their parity-forbidden 4f–4f electronic transitions. Herein, the local electronic structure of Ln³⁺-doped Cs₂NaInCl₆ DPs is unveiled. Benefiting from the localized electrons of [YbCl₆]³⁻ octahedron in Cs₂NaInCl₆ DPs, an efficient strategy of Cl⁻-Yb³⁺ charge transfer sensitization is proposed to obtain intense near-infrared (NIR) luminescence of Ln³⁺. NIR photoluminescence (PL) quantum yield (QY) up to 39.4% of Yb³⁺ in Cs₂NaInCl₆ is achieved, which is more than three orders of magnitude higher than that (0.1%) in the well-established Cs₂AgInCl₆ via conventional self-trapped excitons sensitization. Density functional theory calculation and Bader charge analysis indicate that the [YbCl₆]³⁻ octahedron is strongly localized in Cs₂NaInCl₆:Yb³⁺, which facilitates the Cl⁻-Yb³⁺ charge transfer process. The Cl⁻-Yb³⁺ charge transfer sensitization mechanism in Cs₂NaInCl₆:Yb³⁺ is further verified by temperature-dependent steady-state and transient PL spectra. Furthermore, efficient NIR emission of Er³⁺ with the NIR PLQY of 7.9% via the Cl⁻-Yb³⁺ charge transfer sensitization is realized. These findings provide fundamental insights into the optical manipulation of Ln³⁺-doped halide DPs, thus laying a foundation for the future design of efficient NIR-emitting DPs.

1. Introduction

Lead-free double perovskites (DPs) with A₂B^IB^{III}X₆ stoichiometry have attracted much attention in recent years due to their good stability, low toxicity, and diversity of composition.^[1] These DPs are characterized by a 3D structure composed of alternating [B⁺X₆] and [B³⁺X₆] corner-sharing octahedron with A⁺ ions occupying the voids. Several combinations for A₂B^IB^{III}X₆ DPs have been reported, wherein B⁺ can be Ag⁺, Na⁺, Li⁺, K⁺ and B³⁺ can be In³⁺, Sb³⁺, Bi³⁺, Tl³⁺, etc.^[2] Despite the attractive photophysical properties of these A₂B^IB^{III}X₆ DPs, their studies were mainly restricted to the visible spectral region. Hitherto, it is quite challenging to realize efficient near-infrared (NIR) luminescence in these DPs.

To this regard, lanthanide ions (e.g., Yb³⁺, Er³⁺, Tm³⁺) with rich electronic energy levels were proposed for tailoring the optical performances of DPs toward the NIR regions. Among various A₂B^IB^{III}X₆ DPs, Cs₂Na(Ag)InCl₆ DPs have been widely reported as one of the excellent hosts for Ln³⁺ doping owing to the direct bandgap

S. Han, D. Tu, Y. Zhang, J. Li, Y. Pei, J. Xu, Z. Gong, X. Chen
CAS Key Laboratory of Design and Assembly of Functional Nanostructures
Fujian Key Laboratory of Nanomaterials and State Key Laboratory of Structural Chemistry
Fujian Institute of Research on the Structure of Matter
Chinese Academy of Sciences
Fuzhou, Fujian 350002, China
E-mail: dttu@fjirsm.ac.cn; xchen@fjirsm.ac.cn

S. Han, D. Tu, X. Chen
University of Chinese Academy of Sciences
Beijing 100049, China
D. Tu, J. Xu, X. Chen
Fujian Science & Technology Innovation Laboratory for Optoelectronic Information of China
Fuzhou, Fujian 350108, China
Z. Xie
College of Mechanical and Electronic Engineering
Fujian Agriculture and Forestry University
Fuzhou, Fujian 350002, China

 The ORCID identification number(s) for the author(s) of this article can be found under <https://doi.org/10.1002/advs.202203735>

© 2022 The Authors. Advanced Science published by Wiley-VCH GmbH. This is an open access article under the terms of the Creative Commons Attribution License, which permits use, distribution and reproduction in any medium, provided the original work is properly cited.

DOI: 10.1002/advs.202203735

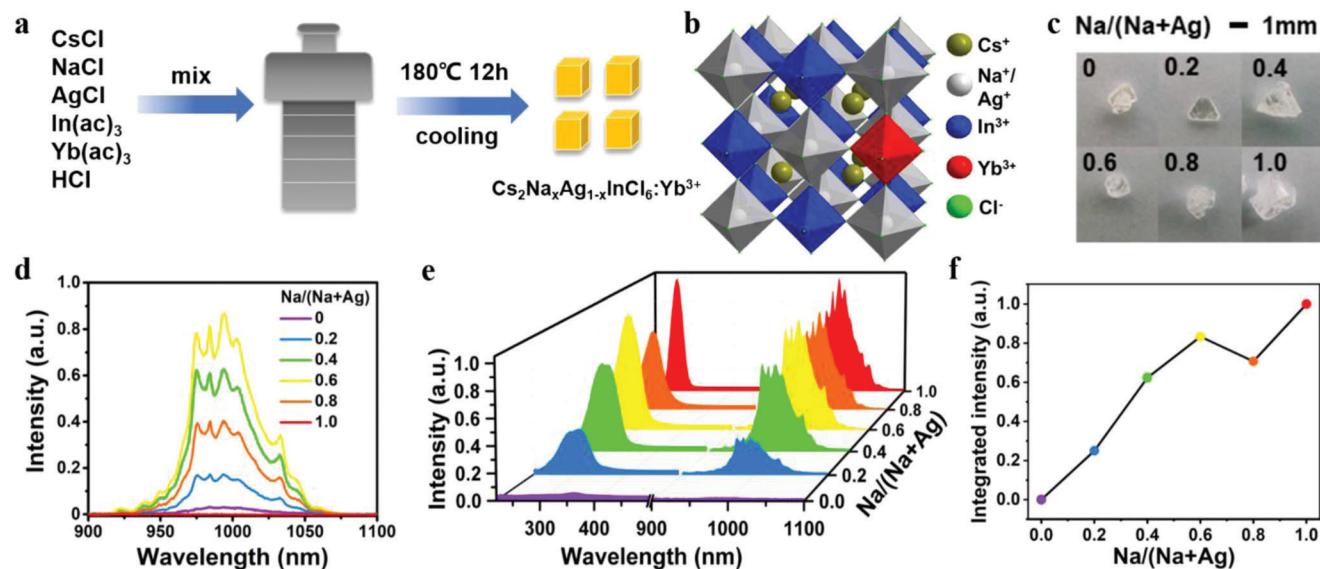


Figure 1. a) Schematic diagram of the synthesis of $\text{Cs}_2\text{Na}_x\text{Ag}_{1-x}\text{InCl}_6$ and $\text{Cs}_2\text{Na}_x\text{Ag}_{1-x}\text{InCl}_6:\text{Yb}^{3+}$ crystals with different $\text{Na}/(\text{Na}+\text{Ag})$ ratios. b) Crystal structure of $\text{Cs}_2\text{Na}_x\text{Ag}_{1-x}\text{InCl}_6:\text{Yb}^{3+}$. c) Photographs of $\text{Cs}_2\text{Na}_x\text{Ag}_{1-x}\text{InCl}_6:\text{Yb}^{3+}$ crystals. d) PL emission spectra of $\text{Cs}_2\text{Na}_x\text{Ag}_{1-x}\text{InCl}_6:\text{Yb}^{3+}$ crystals excited by 365 nm. e) PL excitation (left) and emission (right) spectra of $\text{Cs}_2\text{Na}_x\text{Ag}_{1-x}\text{InCl}_6:\text{Yb}^{3+}$ crystals. f) Integrated emission intensity of Yb^{3+} in $\text{Cs}_2\text{Na}_x\text{Ag}_{1-x}\text{InCl}_6:\text{Yb}^{3+}$ crystals with different $\text{Na}/(\text{Na}+\text{Ag})$ ratios.

character and high chemical stability. It was reported that NIR emission from Yb^{3+} can be produced in $\text{Cs}_2\text{AgInCl}_6$ DPs via the sensitization of self-trapped exciton (STE).^[3] For example, Kim et al. doped $\text{Yb}^{3+}/\text{Er}^{3+}$ into $\text{Cs}_2\text{AgInCl}_6$ nanocrystals, which exhibited characteristic NIR emissions of Yb^{3+} and Er^{3+} peaking at 996 and 1537 nm, respectively.^[4] However, the NIR photoluminescence (PL) quantum yield (QY) of these Ln^{3+} -doped $\text{Cs}_2\text{AgInCl}_6$ DPs remains low (<5%). Thus, substantial efforts have been made to overcome such obstacles and to enhance the NIR luminescence of Ln^{3+} -doped DPs. Typically, sensitizer (e.g., Bi^{3+}) co-doping or Na^+/Ag^+ alloying strategies have to be adopted. Nag et al. boosted the NIR emission of Ln^{3+} in $\text{Cs}_2\text{AgInCl}_6$ through co-doping with Bi^{3+} , which introduced a new optical absorption channel to sensitize the Ln^{3+} dopants of Yb^{3+} and Er^{3+} .^[5] Lin et al. synthesized $\text{Bi}^{3+}/\text{Yb}^{3+}$ co-doped $\text{Cs}_2\text{Na}_{0.6}\text{Ag}_{0.4}\text{InCl}_6$ DPs, in which Na^+/Ag^+ alloying broke the local site symmetry of $\text{Cs}_2\text{AgInCl}_6$ to enhance the NIR emission of Bi^{3+} -sensitized Yb^{3+} .^[6] Because the optical transitions of Ln^{3+} are sensitive to the local coordination, the PLQY of Ln^{3+} ions in these lead-free DPs strongly depends on the crystal structure around Ln^{3+} . Unfortunately, the local electronic structure of Ln^{3+} -doped $\text{Cs}_2\text{NaInCl}_6$ and $\text{Cs}_2\text{AgInCl}_6$ DPs remains essentially untouched yet. To circumvent the complicated energy transfer procedures and difficulty of composition regulation, an unambiguous local structural analysis is a prerequisite to optimizing their optical performance for further applications.

Herein, we propose a facile strategy to boost the NIR luminescence of Ln^{3+} (Yb^{3+} and Er^{3+}) in $\text{Cs}_2\text{NaInCl}_6$ DPs. Through a theoretical survey of the local electronic structure based on density functional theory (DFT) and Bader charge analysis calculations, we revealed that the characteristic local electronic structure of $[\text{YbCl}_6]^{3-}$ octahedron in $\text{Cs}_2\text{NaInCl}_6$ DPs can greatly promote the Cl^- - Yb^{3+} charge transfer process. Benefiting from the Cl^- - Yb^{3+} charge transfer sensitization, intense NIR emission of Yb^{3+}

in $\text{Cs}_2\text{NaInCl}_6$ DPs was achieved, with an intensity 142.2 times higher than the well-established $\text{Cs}_2\text{AgInCl}_6:\text{Yb}^{3+}$ counterparts. Temperature-dependent PL spectroscopic measurements confirmed the efficient energy transfer path from Cl^- - Yb^{3+} charge transfer band (CTB) to Yb^{3+} .^[7] Furthermore, we also achieved intense NIR emission of Er^{3+} in $\text{Cs}_2\text{NaInCl}_6:\text{Yb}^{3+}/\text{Er}^{3+}$ through Cl^- - Yb^{3+} charge transfer sensitization, the integrated intensity of which was 1510.2 times higher than that of $\text{Cs}_2\text{NaInCl}_6:\text{Er}^{3+}$ counterparts, respectively.

2. Results and Discussion

$\text{Cs}_2\text{Na}_x\text{Ag}_{1-x}\text{InCl}_6$ and $\text{Cs}_2\text{Na}_x\text{Ag}_{1-x}\text{InCl}_6:\text{Yb}^{3+}$ crystals with different Na/Ag ratios were synthesized via a hydrothermal method (Figure 1a). X-ray diffraction (XRD) patterns of the crystals can be well indexed into cubic $\text{Cs}_2\text{AgInCl}_6$ (ICSD No. 244519) and $\text{Cs}_2\text{NaInCl}_6$ (ICSD No. 132718) without any impurities (Figure S1, Supporting Information), which indicates that the as-prepared $\text{Cs}_2\text{Na}_x\text{Ag}_{1-x}\text{InCl}_6:\text{Yb}^{3+}$ crystals have the typical double perovskite structure with space group of $Fm\bar{3}m$ (Figure 1b). These crystals were transparent with the size of several millimeters (Figure 1c). The absorption band of $\text{Cs}_2\text{Na}_x\text{Ag}_{1-x}\text{InCl}_6:\text{Yb}^{3+}$ crystals located in the UV region, and band edges monotonically shifted from 355 to 283 nm as the $\text{Na}/(\text{Na}+\text{Ag})$ ratio increased from 0 to 1 (Figure S2, Supporting Information).

Upon excitation at 365 nm, NIR emission of Yb^{3+} can be produced in these $\text{Cs}_2\text{Na}_x\text{Ag}_{1-x}\text{InCl}_6:\text{Yb}^{3+}$ DPs. The optimal NIR emission of Yb^{3+} was obtained when $\text{Na}/(\text{Na}+\text{Ag})$ ratio was 0.6 as reported previously (Figure 1d).^[3a,8] However, it should be noted that the excitation peaks exhibited an obvious blue shift from 350 to 273 nm and the shape of the peaks became sharper with the $\text{Na}/(\text{Na}+\text{Ag})$ ratio rising from 0 to 1 (Figure 1e). Upon excitation with the best excitation wavelength of these $\text{Cs}_2\text{Na}_x\text{Ag}_{1-x}\text{InCl}_6:\text{Yb}^{3+}$ DPs, it was observed that the NIR lumi-

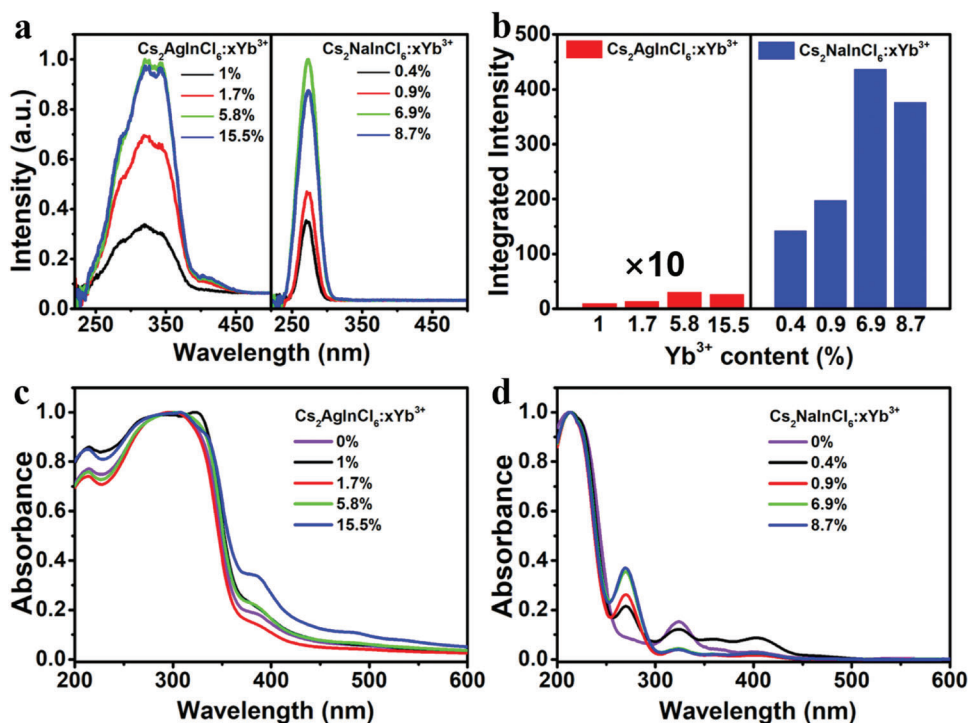


Figure 2. a) PL excitation spectra of Cs₂AgInCl₆:Yb³⁺ and Cs₂NaInCl₆:Yb³⁺ with different Yb³⁺ concentrations. b) Integrated Yb³⁺ emission intensity of Cs₂AgInCl₆:Yb³⁺ and Cs₂NaInCl₆:Yb³⁺ with different Yb³⁺ concentrations. c) Diffuse reflectance spectra of Cs₂AgInCl₆:Yb³⁺ with different Yb³⁺ concentrations. d) Diffuse reflectance spectra of Cs₂NaInCl₆:Yb³⁺ with different Yb³⁺ concentrations.

nescence intensity of Yb³⁺ markedly increased by 135.6 times as the Na/(Na+Ag) ratio increased from 0 to 1 (Figure 1f). According to the PL decays of Yb³⁺, the lifetime of Yb³⁺ increased from 2.72 to 4.52 ms with increasing the Na/(Na+Ag) ratio from 0 to 1 (Figure S2, Supporting Information). Intriguingly, Cs₂NaInCl₆:Yb³⁺ exhibited the highest NIR luminescence intensity and longest PL lifetime of Yb³⁺ among the Cs₂Na_xAg_{1-x}InCl₆:Yb³⁺ DPs, which had not been reported before.

To explore the NIR luminescence mechanism of Yb³⁺ in Cs₂AgInCl₆ and Cs₂NaInCl₆, we synthesized Cs₂AgInCl₆:Yb³⁺ and Cs₂NaInCl₆:Yb³⁺ DPs with different contents of Yb³⁺. XRD patterns confirmed the pure phase of these samples (Figure S3, Supporting Information). X-ray photoelectron spectra analysis revealed the existence of Yb³⁺ ions in the as-prepared DPs (Figure S4, Supporting Information). For Cs₂AgInCl₆, the feeding concentrations of Yb³⁺ were from 50% to 200%, while the actual Yb³⁺ concentrations in the crystal lattice were identified to be only from 1% to 15.5% based on the inductively coupled plasma atomic emission spectra analysis (Table S1, Supporting Information).^[3a] By monitoring the Yb³⁺ emission at 994 nm, a broad excitation band (250–400 nm) centered at ≈350 nm was detected (Figure 2a), which was associated with the bandgap absorption of Cs₂AgInCl₆. Upon excitation at 365 nm, Cs₂AgInCl₆:Yb³⁺ with different Yb³⁺ concentrations exhibited weak NIR PL (Figure S5, Supporting Information and Figure 2b). PL decays revealed decreased PL lifetime from 2.76 to 2.54 ms with the concentration of Yb³⁺ from 1.0% to 15.5% (Figure S5, Supporting Information). Diffuse reflectance spectra of Cs₂AgInCl₆:Yb³⁺ exhibited an intense absorption at ≈358 nm (3.47 eV) (Fig-

ure 2c), which agrees well with the absorption spectrum of pure Cs₂AgInCl₆.^[2b]

For Cs₂NaInCl₆, we adopted the same feeding concentrations as those in Cs₂AgInCl₆, resulting in also low concentrations of Yb³⁺ from 0.4% to 8.7% into the Cs₂NaInCl₆ lattice (Tables S2 and S3, Supporting Information). When monitoring the Yb³⁺ emission of 994 nm, a sharp excitation peak at 273 nm was detected, which was ≈70 nm blue-shift compared with that of Cs₂AgInCl₆:Yb³⁺ (Figure 2a). Meanwhile, the full-width of half-maximum (FWHM) of the excitation peak (≈30 nm) was much narrower than that (≈60 nm) of Cs₂AgInCl₆:Yb³⁺. Diffuse reflectance spectrum of pure Cs₂NaInCl₆ exhibited an ultra-weak absorption band in the visible region and the bandgap was determined to be 4.45 eV (Figure 2d).^[2f,9] However, a new and sharp absorption peak appeared at ≈273 nm when Yb³⁺ was introduced in Cs₂NaInCl₆. With increasing the Yb³⁺ concentration, this absorption peak increased and reached the strongest when the Yb³⁺ concentration was 6.9%. According to the previous report, this sharp excitation peak can be well conformed to the CTB absorption.^[10] Particularly, upon excitation at 273 nm, the NIR luminescence intensity of Yb³⁺ was observed to be 142.2 times higher than that of the Cs₂AgInCl₆:Yb³⁺ counterpart with the optimal doping concentration (Figure 2b). The highest PLQY of Yb³⁺ in Cs₂NaInCl₆:Yb³⁺ reaches 39.4%, which is higher than most of the lead-free halide DPs (Table S4, Supporting Information). Note that the NIR PLQY of Cs₂AgInCl₆:Yb³⁺ counterpart was less than 0.1% under otherwise identical conditions. Furthermore, the PL lifetime of Yb³⁺ in Cs₂NaInCl₆:Yb³⁺ was determined to decrease from 4.54 to 4.11 ms with the increase of Yb³⁺

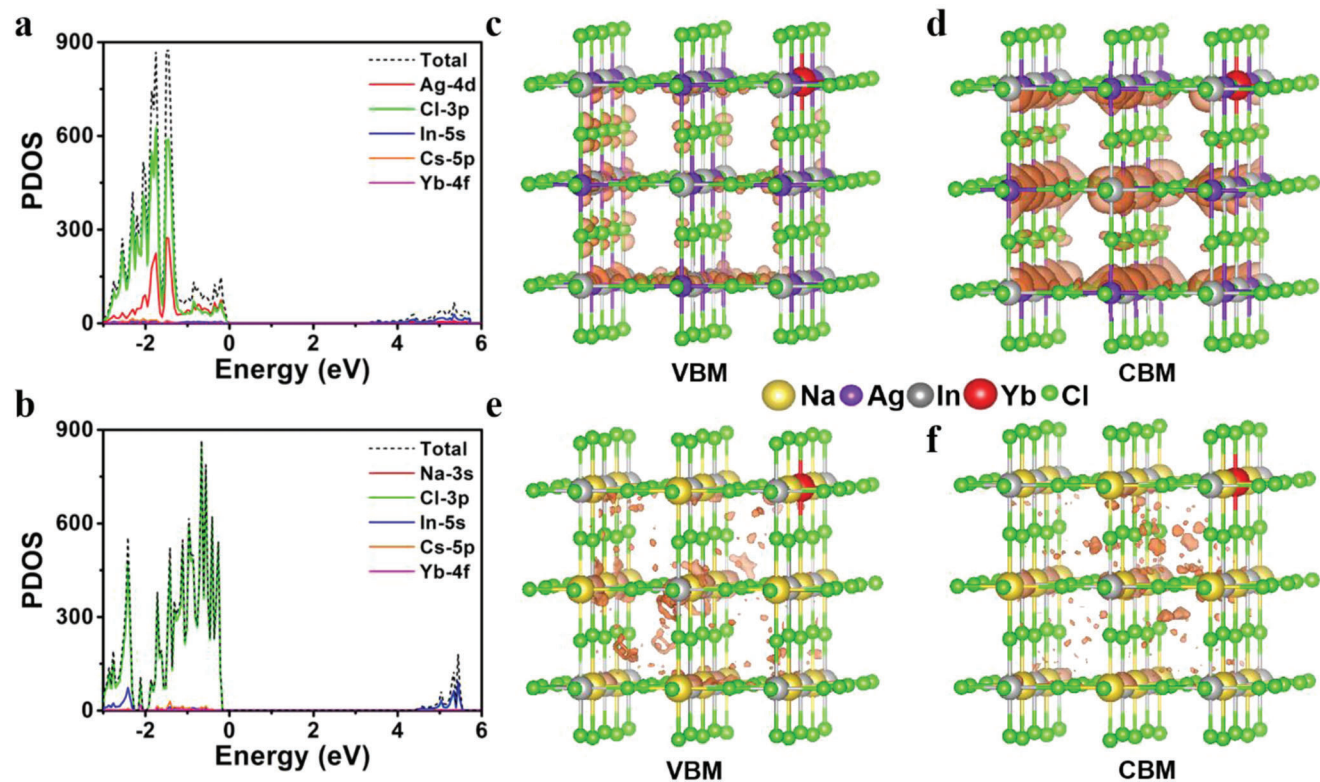


Figure 3. Partial density of states for a) $\text{Cs}_2\text{AgInCl}_6:\text{Yb}^{3+}$ and b) $\text{Cs}_2\text{NaInCl}_6:\text{Yb}^{3+}$. Orbital distribution profiles of c) VBM and d) CBM in $\text{Cs}_2\text{AgInCl}_6:\text{Yb}^{3+}$ (Cs atoms are not displayed). Orbital distribution profiles of e) VBM and f) CBM in $\text{Cs}_2\text{NaInCl}_6:\text{Yb}^{3+}$ (Cs atoms are not displayed).

concentration from 0.4% to 8.7% (Figure S5, Supporting Information), which was much longer than that in $\text{Cs}_2\text{AgInCl}_6:\text{Yb}^{3+}$.

To shed more light on the NIR luminescent mechanism of Yb^{3+} , first-principles calculations based on hybrid DFT were carried out. We replaced the central In^{3+} ion with Yb^{3+} ion in a $2 \times 2 \times 2$ supercell of $\text{Cs}_2\text{AgInCl}_6:\text{Yb}^{3+}$ and $\text{Cs}_2\text{NaInCl}_6:\text{Yb}^{3+}$ (Figure S8, Supporting Information). The bandgaps of $\text{Cs}_2\text{AgInCl}_6:\text{Yb}^{3+}$ and $\text{Cs}_2\text{NaInCl}_6:\text{Yb}^{3+}$ were determined to be 3.21 and 4.38 eV, respectively, wherein Yb^{3+} made no contributions to the valence band maximum (VBM) or conduction band minimum (CBM) (Figure 3a,b). The partial density of states analysis and orbital distribution profiles of $\text{Cs}_2\text{AgInCl}_6:\text{Yb}^{3+}$ showed that VBM was composed of mixed configuration of Ag 4d and Cl 3p states, and CBM mainly consisted of In 5s states with minor contributions from Ag 4d and Cl 3p states (Figure 3c,d). Such configuration benefited the formation of STE, which resulted from the Jahn–Teller distortion of the connected $[\text{AgCl}_6]^{5-}-[\text{InCl}_6]^{3-}$ octahedron.^[2b] For $\text{Cs}_2\text{NaInCl}_6:\text{Yb}^{3+}$, VBM and CBM were essentially composed of Cl 3p states and In 5s states, respectively, which revealed that the orbitals were distributed over the whole supercell with little spatial overlap (Figure 3e,f). Such poor spatial overlap led to the extremely weak edge-to-edge transition in this system.^[11] From the above partial density of states analysis, it can be seen that Cl 3p states coupled with Ag 4d states in VBM of $\text{Cs}_2\text{AgInCl}_6:\text{Yb}^{3+}$, which thus weakened the coupling of Cl and Yb and may be adverse to the Cl^- - Yb^{3+} charge transfer process in $[\text{YbCl}_6]^{3-}$ octahedron. By contrast, VBM of $\text{Cs}_2\text{NaInCl}_6:\text{Yb}^{3+}$ was mainly composed of Cl 3p states without the contributions

from Na, benefiting the coupling of Cl^- and Yb^{3+} and favoring the Cl^- - Yb^{3+} charge transfer process.

The different electronic structures of $\text{Cs}_2\text{NaInCl}_6:\text{Yb}^{3+}$ and $\text{Cs}_2\text{AgInCl}_6:\text{Yb}^{3+}$ DPs were further verified by Bader charge analysis. In $\text{Cs}_2\text{AgInCl}_6:\text{Yb}^{3+}$, Ag⁺ and Cl⁻ around Yb^{3+} had charge of +0.642 and -0.655, respectively. Besides, $[\text{YbCl}_6]^{3-}$ octahedron had a charge of -2.116, which confirmed that the electron of Cl⁻ ion was delocalized toward Ag⁺ due to the high covalency of the Ag–Cl bond (Figure 4a).^[12] As such, the 3d orbit of Ag⁺ may catch electrons from Cl⁻, which thus impeded the charge transfer from Cl⁻ to Yb^{3+} , as revealed by the electron localization function (ELF) analysis (Figure 4b,c).^[13] By contrast, Na⁺ ion in the $\text{Cs}_2\text{NaInCl}_6:\text{Yb}^{3+}$ almost ionized completely with a charge of +0.857 and neighboring Cl⁻ with a charge of -0.753 (Figure 4a). Meanwhile, $[\text{YbCl}_6]^{3-}$ octahedron had a charge of -2.623, indicating that the electron may localize in the $[\text{YbCl}_6]^{3-}$ octahedron. Moreover, it was determined that the ELF between Na⁺ and Cl⁻ was almost zero due to the ionic bond characteristic (Figure 4e). Such weak interaction between Na and Cl in $\text{Cs}_2\text{NaInCl}_6:\text{Yb}^{3+}$ may greatly promote the Cl^- - Yb^{3+} charge transfer process (Figure 4f).

Furthermore, we carried out temperature-dependent steady-state and transient PL spectroscopic measurements to gain deep insights into the excited-state dynamics of Yb^{3+} in $\text{Cs}_2\text{NaInCl}_6$. For pure $\text{Cs}_2\text{NaInCl}_6$, blue STE emission located at ≈ 450 nm with the FWHM of ≈ 75 nm was observed with temperatures below 200 K (Figure 5a,b). The integrated intensity of STE at 10 K was 26.3 times higher than that at 300 K. Accordingly,

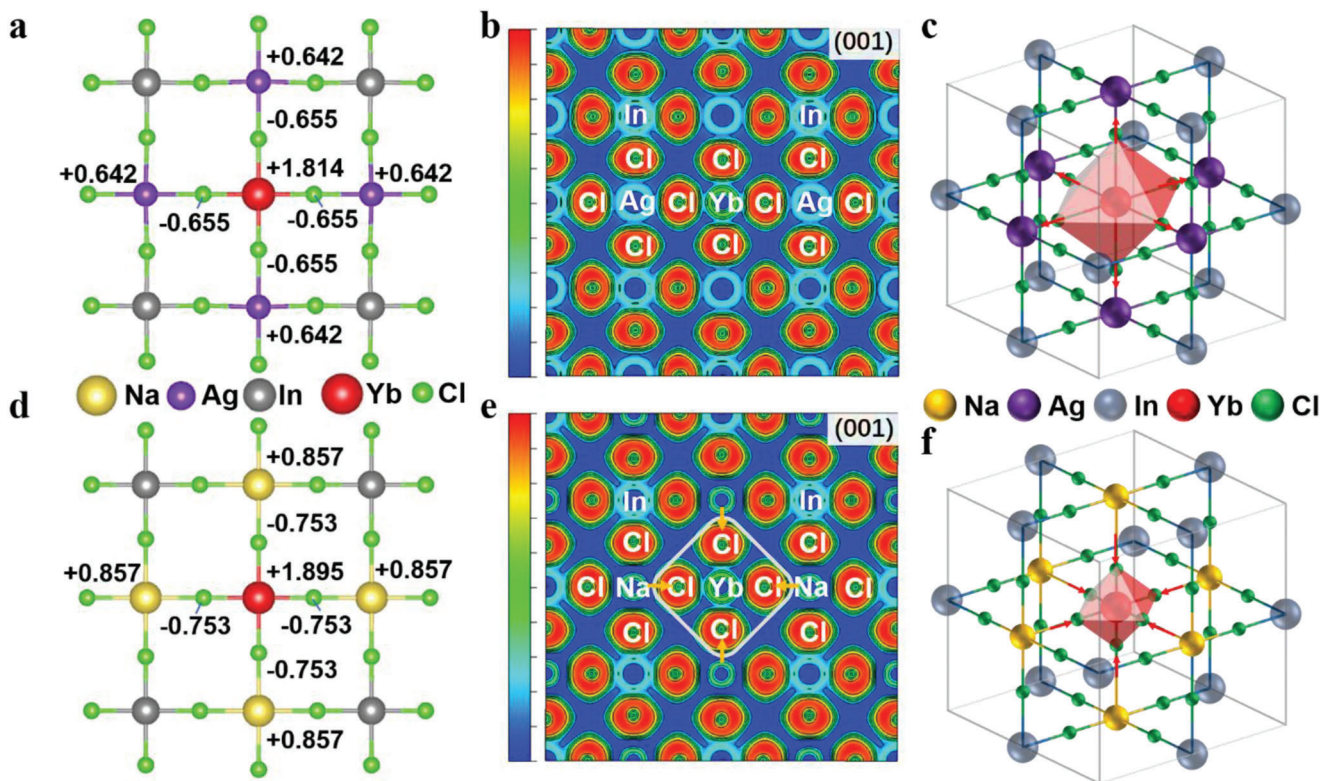


Figure 4. a) Bader charge analysis and b) ELF of Cs₂AgInCl₆:Yb³⁺. c) Schematic diagram of the structure of Cs₂AgInCl₆:Yb³⁺. d) Bader charge analysis and e) ELF of Cs₂NaInCl₆:Yb³⁺. f) Schematic diagram of the structure of Cs₂NaInCl₆:Yb³⁺.

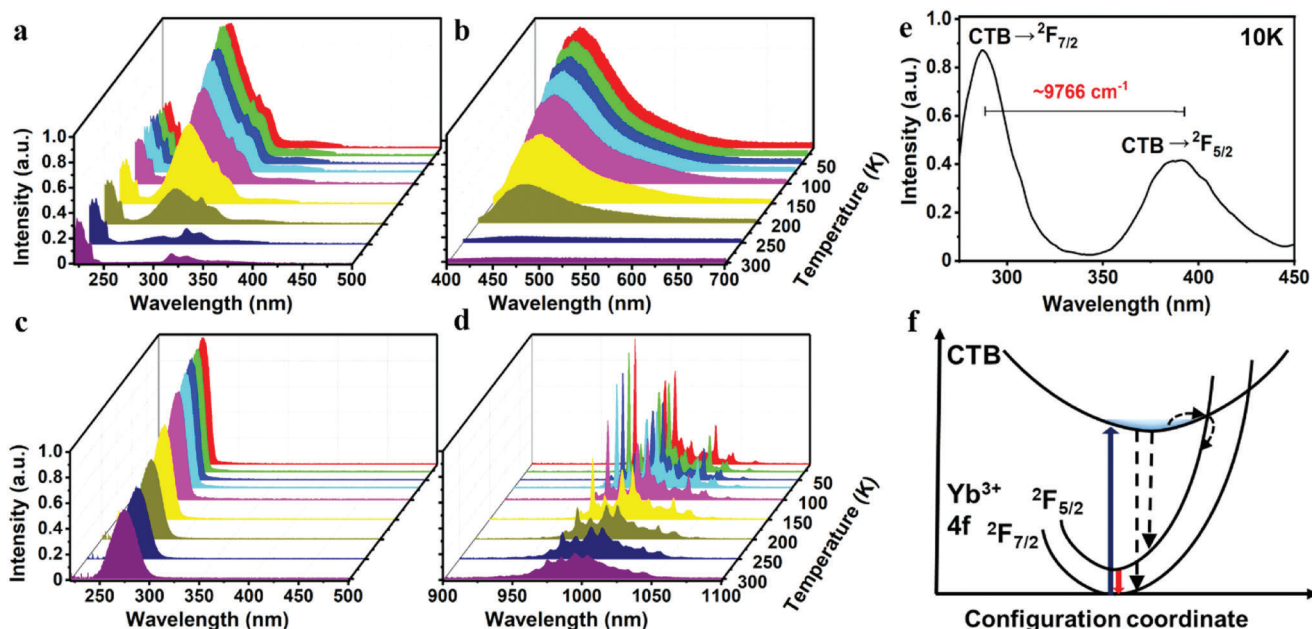


Figure 5. Temperature-dependent a) excitation spectra ($\lambda_{\text{em}} = 450 \text{ nm}$) and b) emission spectra ($\lambda_{\text{ex}} = 290 \text{ nm}$) of Cs₂NaInCl₆. Temperature-dependent c) excitation spectra ($\lambda_{\text{em}} = 994 \text{ nm}$) and d) emission spectra ($\lambda_{\text{ex}} = 273 \text{ nm}$) of Cs₂NaInCl₆:6.9% Yb³⁺. e) PL emission spectra of Cs₂NaInCl₆:6.9% Yb³⁺ at 10 K ($\lambda_{\text{ex}} = 273 \text{ nm}$). f) Schematic illustration of the electronic transitions of Yb³⁺ in Cs₂NaInCl₆.

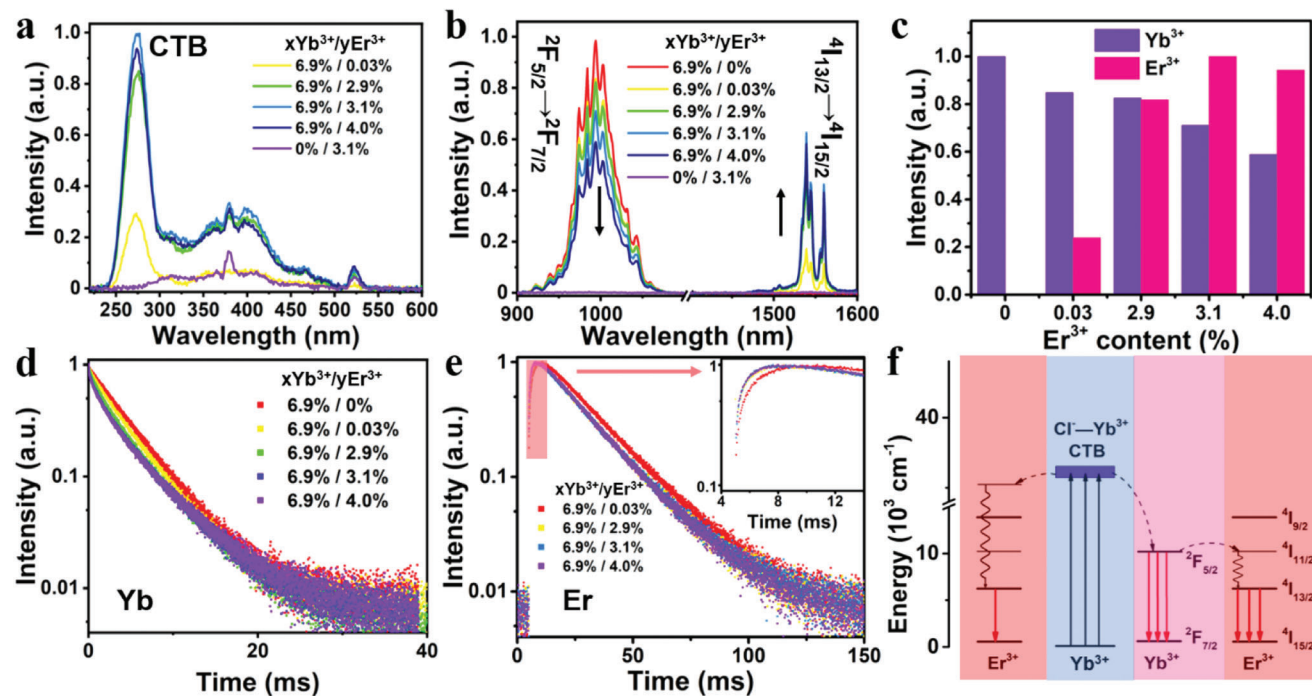


Figure 6. a) Excitation spectra ($\lambda_{em} = 1540$ nm) and b) emission spectra of $\text{Cs}_2\text{NaInCl}_6$ ($\lambda_{ex} = 273$ nm) doped with different contents of Yb^{3+} and Er^{3+} . c) Integrated intensity of Yb^{3+} emission (purple) and Er^{3+} emission (pink) in $\text{Cs}_2\text{NaInCl}_6:6.9\%\text{Yb}^{3+}/\text{Er}^{3+}$ with different contents of Er^{3+} . d) PL decays of Yb^{3+} in $\text{Cs}_2\text{NaInCl}_6:\text{Yb}^{3+}/\text{Er}^{3+}$ with different contents Yb^{3+} and Er^{3+} by monitoring the emission at 994 nm. e) PL decays of Er^{3+} in $\text{Cs}_2\text{NaInCl}_6:\text{Yb}^{3+}/\text{Er}^{3+}$ with different contents Yb^{3+} and Er^{3+} by monitoring the emission at 1540 nm. The initial fast rise portion was enlarged in the inset. f) Schematic diagram of energy transfer process in $\text{Cs}_2\text{NaInCl}_6$ with simplified energy levels of Yb^{3+} and Er^{3+} .

the activation energy was determined to be 76 meV (Figure S6, Supporting Information), indicating excellent thermal stability of $\text{Cs}_2\text{NaInCl}_6$.^[14] The excitation spectra of STE peaking at ≈ 290 nm for $\text{Cs}_2\text{NaInCl}_6$ were associated with the bandgap absorption. Nevertheless, the excitation spectra of Yb^{3+} exhibited sharp peaks ranging from 265 to 273 nm for $\text{Cs}_2\text{NaInCl}_6:\text{Yb}^{3+}$ (Figure 5c), which was distinct from the excitation spectra of pure $\text{Cs}_2\text{NaInCl}_6$, suggesting that they were originated from different processes. Upon excitation at 273 nm, a series of characteristic Yb^{3+} emission peaks were observed (Figure 5d). Besides, several vibronic peaks appeared at temperatures below 200 K, which were attributed to the vibrational modes of $[\text{YbCl}_6]^{3-}$ (Figure S7, Supporting Information).^[15] The PL lifetime of ${}^2\text{F}_{5/2}$ of Yb^{3+} decreased from 8.17 ms at 10 K to 4.54 ms at 300 K due to the thermal quenching at high temperatures (Figure S6, Supporting Information).

Particularly, upon excitation at 273 nm at 10 K, two peaks with an energy gap of ≈ 9766 cm^{-1} were observed for $\text{Cs}_2\text{NaInCl}_6:\text{Yb}^{3+}$, which agreed well with the energy gap between ${}^2\text{F}_{5/2}$ and ${}^2\text{F}_{7/2}$ of Yb^{3+} (Figure 5e). These two peaks can be attributed to the transitions from CTB to ${}^2\text{F}_{7/2}$ (Yb^{3+}) and ${}^2\text{F}_{5/2}$ (Yb^{3+}), respectively.^[10d] Such a result explicitly validated the existence of $\text{Cl}^--\text{Yb}^{3+}$ CTB.^[16] Thus, the energy transfer process of Yb^{3+} in $\text{Cs}_2\text{NaInCl}_6$ was proposed in Figure 5f. Upon UV excitation at 273 nm, the Yb^{3+} ion is excited from the 4f ground state (${}^2\text{F}_{7/2}$) to the $\text{Cl}^--\text{Yb}^{3+}$ CTB, followed by a fast relaxation process to the 4f excited state (${}^2\text{F}_{5/2}$) through thermal activation. Then, intense NIR emission of Yb^{3+} at 994 nm can be detected due to the radiative transition from ${}^2\text{F}_{5/2}$ to ${}^2\text{F}_{7/2}$.

Besides Yb^{3+} , another Ln^{3+} dopant, Er^{3+} , was employed to produce NIR emissions (Table S5, Supporting Information). **Figure 6a** shows the PL excitation spectra of Er^{3+} singly doped and $\text{Yb}^{3+}/\text{Er}^{3+}$ co-doped $\text{Cs}_2\text{NaInCl}_6$ DPs. By monitoring the Er^{3+} emission at 1540 nm, the excitation peaks at 380 and 520 nm were detected for $\text{Cs}_2\text{NaInCl}_6:\text{Er}^{3+}$ DPs, which belonged to ${}^4\text{I}_{15/2} \rightarrow {}^4\text{G}_{11/2}$ and ${}^4\text{I}_{15/2} \rightarrow {}^2\text{H}_{11/2}$ transitions of Er^{3+} , respectively. For $\text{Cs}_2\text{NaInCl}_6:\text{Yb}^{3+}/\text{Er}^{3+}$ DPs, a strong peak at 273 nm corresponding to the $\text{Cl}^--\text{Yb}^{3+}$ CTB excitation appeared beside the above-mentioned excitation peaks of Er^{3+} . Upon excitation at 273 nm, $\text{Cs}_2\text{NaInCl}_6:\text{Yb}^{3+}/\text{Er}^{3+}$ DPs showed strong NIR emission peaking at 994 and 1540 nm corresponding to the ${}^2\text{F}_{5/2} \rightarrow {}^2\text{F}_{7/2}$ transition of Yb^{3+} and ${}^4\text{I}_{13/2} \rightarrow {}^4\text{I}_{15/2}$ of Er^{3+} , respectively (Figure 6b). Note that the optimal integrated NIR intensity of $\text{Cs}_2\text{NaInCl}_6:\text{Yb}^{3+}/\text{Er}^{3+}$ DPs was 1510.2 times higher than that of $\text{Cs}_2\text{NaInCl}_6:\text{Er}^{3+}$ counterparts (Figure 6b,c). The highest NIR PLQY of $\text{Cs}_2\text{NaInCl}_6:\text{Yb}^{3+}/\text{Er}^{3+}$ DPs was determined to be 7.9% (Table S4, Supporting Information).

Moreover, with the increase of Er^{3+} concentration in $\text{Cs}_2\text{NaInCl}_6:6.9\%\text{Yb}^{3+}/\text{xEr}^{3+}$ DPs, it was discovered that the integrated intensity of Er^{3+} emission continuously increased while the Yb^{3+} emission steadily decreased, indicative of the energy transfer from Yb^{3+} to Er^{3+} . Meanwhile, the PL lifetime of Yb^{3+} in $\text{Cs}_2\text{NaInCl}_6:6.9\%\text{Yb}^{3+}/\text{xEr}^{3+}$ DPs decreased from 4.29 to 3.06 ms with the content of Er^{3+} increasing from 0.03% to 4.0%, which also verified the enhanced energy transfer from Yb^{3+} to Er^{3+} (Figure 6d). Furthermore, a decreased rising edge from 4.71 to 2.14 ms can be observed from the PL decays of Er^{3+} by monitoring the emission at 1540 nm, revealing the faster

electron population process with increasing content of Er^{3+} (Figure 6e). The energy transfer efficiency (η_{ET}) can be calculated as^[17]

$$\eta_{\text{ET}} = 1 - \frac{\tau_s}{\tau_0} \quad (1)$$

where τ_0 and τ_s display the Yb^{3+} lifetime (monitored at 994 nm) in the absence and presence of Er^{3+} , respectively. Based on effective lifetime changes of different content Er^{3+} -doped $\text{Cs}_2\text{NaInCl}_6:6.9\%\text{Yb}^{3+}/x\text{Er}^{3+}$ DPs, η_{ET} were calculated to be 11.3%, 23.4%, 29.5%, and 29.7% with the Er^{3+} content of 0.03%, 2.9%, 3.1%, and 4.0%, respectively. Thus, the energy transfer mechanism in $\text{Cs}_2\text{NaInCl}_6:\text{Yb}^{3+}/\text{Er}^{3+}$ is illustrated in Figure 6f. Upon excitation to the $\text{Cl}^--\text{Yb}^{3+}$ CTB, the excitation energy is transferred to the $^2\text{F}_{5/2}$ (Yb^{3+}) level through a fast non-radiative relaxation process, followed by the radiative transition of Yb^{3+} at 994 nm and energy transfer to the well-matched $^4\text{I}_{11/2}$ level of Er^{3+} . Through the nonradiative relaxation from $^4\text{I}_{11/2}$ to $^4\text{I}_{13/2}$, the NIR emission at 1540 nm can be produced due to the $^4\text{I}_{13/2} \rightarrow ^4\text{I}_{15/2}$ transition of Er^{3+} .

3. Conclusion

In summary, we have unveiled the different local electronic structures of Ln^{3+} ions-doped $\text{Cs}_2\text{NaInCl}_6$ DPs. Accordingly, a novel strategy for achieving efficient NIR luminescence of Ln^{3+} in $\text{Cs}_2\text{NaInCl}_6$ DPs was proposed, resulting in an NIR PLQY up to 39.4% of Yb^{3+} by virtue of the $\text{Cl}^--\text{Yb}^{3+}$ charge transfer sensitization. Through systematically investigating the PL excitation and emission spectra of $\text{Cs}_2\text{AgInCl}_6:\text{Yb}^{3+}$ and $\text{Cs}_2\text{NaInCl}_6:\text{Yb}^{3+}$, we revealed the superior sensitization paths of NIR emission of Yb^{3+} in $\text{Cs}_2\text{NaInCl}_6$ relative to that in $\text{Cs}_2\text{AgInCl}_6$. Notably, the $\text{Cs}_2\text{NaInCl}_6:\text{Yb}^{3+}$ exhibited 142.2 times higher NIR PL intensity than the $\text{Cs}_2\text{AgInCl}_6:\text{Yb}^{3+}$ counterparts. Temperature-dependent PL excitation and emission spectra verified that the proposed $\text{Cl}^--\text{Yb}^{3+}$ charge transfer sensitization mechanism benefited from the localized electrons of $[\text{YbCl}_6]^{3-}$ octahedron in $\text{Cs}_2\text{NaInCl}_6:\text{Yb}^{3+}$, which was also confirmed by the theoretical analysis. Furthermore, efficient NIR luminescence from Er^{3+} with PLQY of 7.9% was also achieved in $\text{Yb}^{3+}/\text{Er}^{3+}$ co-doped $\text{Cs}_2\text{NaInCl}_6$ DPs due to the energy transfer from the $\text{Cl}^--\text{Yb}^{3+}$ CTB to Er^{3+} . These findings provide a universal approach for the development of highly efficient Ln^{3+} -doped NIR luminescent halide DPs, which might pave a new way to manipulate the optical properties of Ln^{3+} -doped DPs toward versatile applications.

Supporting Information

Supporting Information is available from the Wiley Online Library or from the author.

Acknowledgements

This work was supported by the National Natural Science Foundation of China (nos. U1805252, 21975257, 12074380, 12004384, 22135008), the Key Research Program of the Chinese Academy of Sciences (no. ZDRW-CN-2021-3), the CAS/SAFEA International Partnership Program for Creative Research Teams, Natural Science Foundation of Fujian Province (no. 2021L3024, 2019J01403).

Conflict of Interest

The authors declare no conflict of interest.

Data Availability Statement

The data that support the findings of this study are available from the corresponding author upon reasonable request.

Keywords

charge transfer, double perovskites, lanthanide ions, local electronic structure, near-infrared luminescence

Received: June 29, 2022

Revised: August 29, 2022

Published online: September 30, 2022

- [1] a) Z. W. Xiao, Z. N. Song, Y. F. Yan, *Adv. Mater.* **2019**, *31*, 1803792; b) W. W. Meng, X. M. Wang, Z. W. Xiao, J. B. Wang, D. B. Mitzi, Y. F. Yan, *J. Phys. Chem. Lett.* **2017**, *8*, 2999; c) R. Ahmad, G. V. Nutan, D. Singh, G. Gupta, U. Soni, S. Sapra, R. Srivastava, *Nano Res.* **2021**, *14*, 1126; d) Y. Yuan, G. H. Yan, Z. W. Li, B. Q. Jiang, Z. C. Liang, H. J. Fan, W. J. Mai, *Sci. China Mater.* **2021**, *65*, 442; e) T. T. Tran, J. R. Panella, J. R. Chamorro, J. R. Morey, T. M. McQueen, *Mater. Horiz.* **2017**, *4*, 688; f) B. Yang, F. Hong, J. S. Chen, Y. X. Tang, L. Yang, Y. B. Sang, X. S. Xia, J. W. Guo, H. X. He, S. Q. Yang, W. Q. Deng, K. L. Han, *Angew. Chem., Int. Ed.* **2019**, *58*, 2278.
- [2] a) F. Locardi, M. Cirignano, D. Baranov, Z. Dang, M. Prato, F. Drago, M. Ferretti, V. Pinchetti, M. Fanciulli, S. Brovelli, L. De Trizio, L. Manna, *J. Am. Chem. Soc.* **2018**, *140*, 12989; b) J. J. Luo, X. M. Wang, S. R. Li, J. Liu, Y. M. Guo, G. D. Niu, L. Yao, Y. H. Fu, L. Gao, Q. S. Dong, C. Y. Zhao, M. Y. Leng, F. S. Ma, W. X. Liang, L. D. Wang, S. Y. Jin, J. B. Han, L. J. Zhang, J. B. Wang, Y. F. Yan, E. H. Sargent, J. Tang, *Nature* **2018**, *563*, 541; c) B. Yang, X. Mao, F. Hong, W. W. Meng, Y. X. Tang, X. S. Xia, S. Q. Yang, W. Q. Deng, K. L. Han, *J. Am. Chem. Soc.* **2018**, *140*, 17001; d) Y. Liu, Y. Y. Jing, J. Zhao, Q. L. Liu, Z. G. Xia, *Chem. Mater.* **2019**, *31*, 3333; e) P. G. Han, X. Mao, S. Q. Yang, F. Zhang, B. Yang, D. H. Wei, W. Q. Deng, K. L. Han, *Angew. Chem., Int. Ed.* **2019**, *58*, 17231; f) F. Locardi, E. Sartori, J. Buha, J. Zito, M. Prato, V. Pinchetti, M. L. Zaffalon, M. Ferretti, S. Brovelli, I. Infante, L. De Trizio, L. Manna, *ACS Energy Lett.* **2019**, *4*, 1976; g) C. Y. Wang, P. Liang, R. J. Xie, Y. Yao, P. Liu, Y. T. Yang, J. Hu, L. Y. Shao, X. W. Sun, F. Y. Kang, G. D. Wei, *Chem. Mater.* **2020**, *32*, 7814.
- [3] a) S. R. Li, Q. S. Hu, J. J. Luo, T. Jin, J. Liu, J. H. Li, Z. F. Tan, Y. B. Han, Z. Zheng, T. Y. Zhai, H. S. Song, L. Gao, G. D. Niu, J. Tang, *Adv. Opt. Mater.* **2019**, *7*, 1901098; b) Y. Liu, X. M. Rong, M. Z. Li, M. S. Molokeev, J. Zhao, Z. G. Xia, *Angew. Chem., Int. Ed.* **2020**, *59*, 11634; c) Y. Mahor, W. J. Mir, A. Nag, *J. Phys. Chem. C* **2019**, *123*, 15787; d) H. Yin, Q. K. Kong, R. L. Zhang, D. Y. Zheng, B. Yang, K. L. Han, *Sci. China Mater.* **2021**, *64*, 2667.
- [4] W. Lee, S. Hong, S. Kim, *J. Phys. Chem. C* **2019**, *123*, 2665.
- [5] H. Arfin, J. Kaur, T. Sheikh, S. Chakraborty, A. Nag, *Angew. Chem., Int. Ed.* **2020**, *59*, 11307.
- [6] G. D. Zhang, Y. Wei, P. P. Dang, H. Xiao, D. J. Liu, X. K. Li, Z. Y. Cheng, J. Lin, *Dalton Trans.* **2020**, *49*, 15231.
- [7] a) S. Rydberg, M. Engholm, *J. Appl. Phys.* **2013**, *113*, 223510; b) Y. J. Wang, X. J. Zhou, J. Shen, X. Q. Zhao, B. Wu, S. Jiang, L. Li, *J. Am. Ceram. Soc.* **2016**, *99*, 115.
- [8] Z. C. Zeng, B. L. Huang, X. Wang, L. Lu, Q. Y. Lu, M. Z. Sun, T. Wu, T. F. Ma, J. Xu, Y. S. Xu, S. Wang, Y. P. Du, C. H. Yan, *Adv. Mater.* **2020**, *32*, 2004506.

- [9] J. Zhou, X. M. Rong, P. Zhang, M. S. Molokeev, P. J. Wei, Q. L. Liu, X. W. Zhang, Z. G. Xia, *Adv. Opt. Mater.* **2019**, *7*, 1801435.
- [10] a) X. J. Zhou, M. F. Reid, M. D. Faucher, P. A. Tanner, *J. Phys. Chem. B* **2006**, *110*, 14939; b) L. van Pieterse, A. Meijerink, *J. Alloys Compd.* **2000**, *300*, 426; c) L. Aarts, S. Jaqx, B. M. van der Ende, A. Meijerink, *J. Lumin.* **2011**, *131*, 608; d) L. van Pieterse, M. Heeroma, E. de Heer, A. Meijerink, *J. Lumin.* **2000**, *91*, 177.
- [11] D. Zhu, J. Zito, V. Pinchetti, Z. Dang, A. Olivati, L. Pasquale, A. Tang, M. L. Zaffalon, F. Meinardi, I. Infante, L. De Trizio, L. Manna, S. Brovelli, *ACS Energy Lett.* **2020**, *5*, 1840.
- [12] R. S. Larnba, P. Basera, S. Bhattacharya, S. Sapra, *J. Phys. Chem. Lett.* **2019**, *10*, 5173.
- [13] P. Ghosez, J. P. Michenaud, X. Gonze, *Phys. Rev. B* **1998**, *58*, 6224.
- [14] R. S. Zeng, L. L. Zhang, Y. Xue, B. Ke, Z. Zhao, D. Huang, Q. L. Wei, W. C. Zhou, B. S. Zou, *J. Phys. Chem. Lett.* **2020**, *11*, 2053.
- [15] a) L. X. Ning, P. A. Tanner, S. D. Xia, *Vib. Spectrosc.* **2003**, *31*, 51; b) R. Acevedo, P. A. Tanner, T. Meruane, V. Poblete, *Phys. Rev. B* **1996**, *54*, 3976.
- [16] M. Nikl, A. Yoshikawa, T. Fukuda, *Opt. Mater.* **2004**, *26*, 545.
- [17] P. I. Paulose, G. Jose, V. Thomas, N. V. Unnikrishnan, M. K. R. Warriar, *J. Phys. Chem. Solids* **2003**, *64*, 841.